Progress In Electromagnetics Research, PIER 16, 305–330, 1997

MODELING OF MILLIMETER WAVE BACKSCATTER OF TIME-VARYING SNOWCOVER

S.-E. Shih, K.-H. Ding, J. A. Kong, and Y. E. Yang

Department of Electrical Engineering and Computer Science
Research Laboratory of Electronics
Massachusetts Institute of Technology
Cambridge, MA 02139, U.S.A.

R. E. Davis, J. P. Hardy, and R. Jordan

U.S. Army Cold Regions Research and Engineering Laboratory
Hanover, NH 03755-1290, U.S.A.

1. INTRODUCTION

Seasonal snowcover is a major environmental factor over the earth surface. It imposes impacts on the radiation and energy budget between atmosphere and surface [1]. For hydrologic applications, snow is also a major contributor to runoff in rivers and to ground water resource [2,3]. On the ground, snow is generally inhomogeneous and strati-

fied. Furthermore, the effects of snow metamorphosis typically cause the snow grain size, shape, density, and liquid water content to vary from one stratigraphic layer to another [4]. The time-varying snowpack structure greatly complicates the analysis of electromagnetic wave interactions with snow-covered terrain [5]. Stereological methods have analyzed the undisturbed snow microstructure based on images taken from plane sections of snow specimens [6]. The estimated snow parameters have been used in the study of microwave remote sensing of snow [7]. However, these ground truth measurements are usually laborious and thus very difficult to acquire as time series. Several experiences have been reported in the literature on the millimeter wave interaction with snowcover [8–13] and the diurnal variation of radar signatures of snow [14–16]. Although these investigations indicate that the backscatter of snowcover is strongly influenced by the presence of liquid water, electromagnetic modeling of snow undergoing internal changes, due to metamorphism and phase change, still lacks a systematic study.

Snowcover models have been developed to predict the mechanical, thermal, and optical properties for various applications, such as remote sensing, climate modeling, avalanche forecasting, and hydrology [3]. SNTHERM, a one-dimensional mass and energy balance model of snow physics, was developed at the U.S. Army Cold Regions Research and Engineering Laboratory (CRREL) for predicting temperature profiles within snow and frozen soil [17]. The model is formulated to consider a snowcover over soil with high vertical and time resolutions. The model solves a set of governing equations for the mass and energy balance of the snowpack, subject to meteorologicaly determined boundary conditions at the snow-air interface. In addition to temperature prediction, SNTHERM simulates various bulk physical processes of a snowcover, such as accumulation, densification, ablation, sub-surface melt, and water flow. SNTHERM provides a physical insight into the snow metamorphosis process as well as the evolution of snowpack structure, including temperature, grain size, liquid water content, and stratigraphy, under varying environmental conditions. As we know, these snow parameters significantly affect the electromagnetic sensor response of snowcover; however, they are frequently difficult to obtain from field measurements. In this work we apply SNTHERM to simulate the dynamic variation of a snowcover with observed meteorological data. With the knowledge of these snow properties, the backscatter from snowpack can be derived by solving the dense medium radiative

transfer equations which serve here as our electromagnetic scattering model of snow.

Snow is classified as a dense medium where the assumption of independent scattering used in conventional radiative transfer theory [18] is no longer valid. For densely packed scatterers, such as ice particles in snow, the correlation of particle positions, coherent wave interactions, and effects of dependent scattering have to be considered [18–22]. This deficiency is corrected in the dense medium radiative transfer (DMRT) theory [18, 23, 24]. The DMRT theory has been applied to the remote sensing of snow terrain [24–26]. However, in the previous DMRT models of snowcover, the ice particles are assumed to have no bonding with each other, and the effects of reflection and refraction between the strata of snow are not considered. In this study, we apply a model of cohesive spherical particles [27] to account for the clustering feature of snow grains. It has been demonstrated that the aggregation of scatterers greatly affect the electromagnetic properties of densely packed media [27–29]. In what follows we develop a dynamic scattering model of snowcover, with a more realistic snow microstructure, based on DMRT and SNTHERM. This coupled model is then applied to enable the simulation of temporal radar response of snowcover under changing environmental conditions. In Section 2, the DMRT scattering model of a stratified snowcover with clustered ice grains is developed. The reflection and refraction at the snow-snow interface is taken into consideration. Relevant numerical considerations of boundary conditions and quadrature rules are also discussed in this section. The one-dimensional SNTHERM model is summarized in Section 3. We describe briefly the governing equations for the energy and mass balance of snow, and the physical effects on the model parameters used. We show comparisons of dynamical simulation of SNTHERM and the coupled DMRT and SNTHERM model with concurrently measured ground truth and the time series backscatter measurements, respectively, in Section 4. A summary is presented in Section 5.

2. ELECTROMAGNETIC MODELING OF SNOWCOVER

In this section, a DMRT scattering model of stratified snowcover is developed. Cohesive spherical particles are used to model the metamorphosed snow grains. The reflection and refraction at the snow-snow interface, due to the discontinuity of dielectric properties, are

taken into account by applying appropriate boundary conditions and quadrature rules.

2.1 DMRT Equations for Planar Stratified Snowcover

The snowcover considered here is modeled as a stack of horizontal layers assuming planar boundaries between air-snow, snow-snow, and snow-soil interfaces. The complexities of rough interfaces in the snow structure are ignored in this study. Figure 1 shows the layered geometry used. The uppermost medium ($z > 0$) is air with permittivity ϵ_0 , the layer of thickness d_N represents a stratified snow medium, and the lower half space ($z < -d_N$) is soil with a complex permittivity ϵ_g . Within the l -th snow layer, snow grains are modeled as random clusters of small primary spherical ice particles of radius a_l and with a complex permittivity ϵ_s which totally occupy a volume fraction f_{vl} . A stickiness parameter τ_l [27] is applied to parameterize the clustering behavior of snow grains. The clustered ice particles are randomly distributed within the background medium of complex permittivity ϵ_{bl} .

With the configuration described above, the vector DMRT equation is applied to describe the propagation and scattering of radiation inside the l -th dense medium layer,

$$\begin{aligned}\cos\theta \frac{d}{dz}\overline{I}_l(\theta,\phi,z) &= -\kappa_{el}\overline{I}_l(\theta,\phi,z) \\ &+ \int_0^{2\pi} d\phi' \int_0^{\pi} d\theta' \sin\theta' \overline{\overline{P}}_l(\theta,\phi;\theta',\phi') \cdot \overline{I}_l(\theta',\phi',z)\end{aligned} \tag{1}$$

with $l = 1, 2, \ldots, N$, $0 \le \theta \le \pi$, and $0 \le \phi \le 2\pi$. $\overline{I}_l(\theta,\phi,z)$ represents the 4×1 Stokes vector in the direction (θ,ϕ) , κ_{el} is the extinction coefficient which is a sum of scattering and absorption coefficients, and $\overline{\overline{P}}_l(\theta,\phi;\theta',\phi')$ denotes the 4×4 phase matrix which describes how particles scatter radiation from the direction (θ',ϕ') into the direction (θ,ϕ) . The DMRT equation has a similar form with the conventional radiative transfer equation. In the small particle limit, the phase matrix $\overline{\overline{P}}$ in (1) is of the form of Rayleigh phase matrix, but depends on the effective extinction rate and effective albedo, with the effects of dependent and correlated scattering taken into account [18, 23–26].

Microwave interaction with a snowcover is strongly influenced by the presence of liquid water. For dry snow, the background is air with

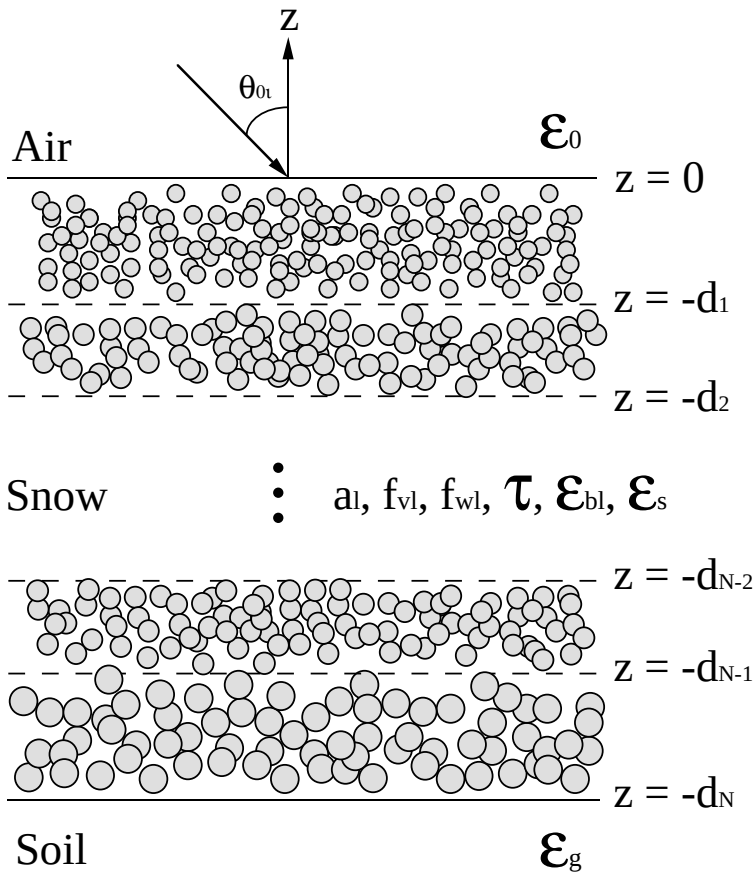

Figure 1. Configuration of an N-layer snowcover.

permittivity ϵ_0. For the case of wet snow, the water inclusions are incorporated as part of the background medium because values are typically a few percent, and snow drains at values more than about 6 percent volume fraction. The water droplets are assumed to be randomly oriented ellipsoids. The dielectric constant of such a "wet air" background is calculated using Polder-van Santen mixing formula [30,31]

$$\epsilon_{bl} = \epsilon_0 + \frac{f_{wl}}{3}(\epsilon_{water} - \epsilon_0) \sum_{i=1}^{3} \frac{\epsilon_{bl}}{\epsilon_{bl} + N_i(\epsilon_{water} - \epsilon_{bl})} \qquad (2)$$

where f_{wl} is the fractional volume of liquid water content or wetness in the l-th snow layer, ϵ_{water} is the complex permittivity of water, ϵ_0 is the permittivity of air, and N_i is the depolarization factor of water particles. In this study the depolarization factor is estimated from the fitting curves given by Hallikainen et al. [30] who show that the depolarization factors not only depend on the shape of water particles, but also the shape depends on the liquid water content.

For dense random media with small spherical particles, the effective wavenumber K calculated using the quasi-crystalline approximation with coherent potential (QCA-CP) is given as [18,25,26]

$$K^2 = k^2 + \frac{f_v(k_s^2 - k^2)}{1 + \frac{k_s^2 - k^2}{3K^2}(1 - f_v)} \left\{ 1 + i \frac{2(k_s^2 - k^2)Ka^3}{9\left[1 + \frac{(k_s^2 - k^2)}{3K^2}(1 - f_v)\right]} \times \left[1 + 4\pi n \int_0^\infty dr\ r^2\,(g(r) - 1)\right] \right\} \tag{3}$$

where k is the wavenumber of background medium, a is the radius of particle, f_v is the fractional volume of scatterers, k_s is the wavenumber of particle, n is the number density of particles, and $g(r)$ is the pair distribution function which describes the correlation between particle positions. In terms of $g(r)$, the effective albedo $\tilde{\omega}$ is obtained as [18, 25, 26]

$$\tilde{\omega} = \frac{2}{9}\frac{a^3 f_v}{\kappa_e} \left| \frac{k_s^2 - k^2}{1 + \frac{k_s^2 - k^2}{3K^2}(1 - f_v)} \right|^2 \left[1 + 4\pi n \int_0^\infty dr\ r^2\,(g(r) - 1)\right] \tag{4}$$

where $\kappa_e = 2K''$ is the extinction coefficient and K'' is the imaginary part of effective propagation constant K.

In a recent work, we have introduced the usage of cohesive particle pair distribution function to describe the particles in clusters [27]. To account for the clustering behavior of ice particles, the cohesive particle model, which assumes the presence of surface cohesion between particles, is applied in this study to simulate snow grains. The cohesion between two particles is described by a dimensionless parameter τ whose inverse is a measure of the attraction or stickiness between particles. The case of $\tau^{-1} = \infty$ corresponds to infinite stickiness and $\tau^{-1} = 0$ corresponds to non-sticky particles. Under the Percus-Yevick (PY) approximation, the pair distribution function for sticky spherical particles has been solved analytically [27]. The integral over pair

distribution function $g(r)$ in (3) and (4) can be obtained in a closed form as

$$4\pi n \int_0^\infty dr\ r^2\,(g(r)-1) = -1 + \frac{(1-f_v)^4}{\left[1+2f_v-\eta f_v(1-f_v)\right]^2} \qquad (5)$$

where the quantity η depends on the stickiness τ and is determined by solving the quadratic equation [27]

$$\frac{f_v}{12}\eta^2 - (\tau + \frac{f_v}{1-f_v})\eta + \frac{1+f_v/2}{(1-f_v)^2} = 0 \qquad (6)$$

2.2 Boundary Conditions and Quadrature Rules

Because the DMRT equation bears a similar form to the conventional radiative transfer equation, the same discrete-ordinate method can be applied to approximate the integral in (1). We use a Gaussian quadrature weighted sum, and then transform the differential-integral equation (1) into a system of coupled first-order differential equations, which is thus solved using the eigenanalysis technique. Additional details can be found in [18]. The reflection and refraction of radiation at the snow-snow interface are calculated according to the stratigraphy of snow, which shows the depth-dependent snow properties. Appropriate boundary conditions and quadrature points and weights are selected in solving the multilayer DMRT equations.

At the uppermost boundary $(z=0)$, the downward going intensity in layer 1 is equal to the sum of refracted incident intensity and reflected upward going intensity

$$\overline{I}_1^-(\pi-\theta_1,\phi_1,z=0) = \overline{\overline{T}}_{01}(\theta_0)\cdot\overline{I}_{0i}(\pi-\theta_0,\phi_0)+\overline{\overline{R}}_{10}(\theta_1)\cdot\overline{I}_1^+(\theta_1,\phi_1,z=0) \qquad (7)$$

where $\overline{I}_{0i}(\pi-\theta_0,\phi_0) = \overline{I}_0\,\delta(\cos\theta_0-\cos\theta_{0i})\,\delta(\phi_0-\phi_{0i})$ is the incident intensity at the direction $(\pi-\theta_{0i},\phi_{0i})$. At the bottom boundary $(z=-d_N)$, the upward going intensity matches the reflected downward going intensity,

$$\overline{I}_N^+(\theta_N,\phi_N,z=-d_N) = \overline{\overline{R}}_{N(N+1)}(\theta_N)\cdot\overline{I}_N^-(\pi-\theta_N,\phi_N,z=-d_N) \qquad (8)$$

At the other interfaces $z = -d_l$, $l = 1, 2, \ldots, N-1$, the boundary conditions for the upward and downward going intensities are given by

$$\overline{I}_{l+1}^{-}(\pi - \theta_{l+1}, \phi_{l+1}, z = -d_l) = \overline{\overline{T}}_{l(l+1)}(\theta_l) \cdot \overline{I}_{l}^{-}(\pi - \theta_l, \phi_l, z = -d_l) + \overline{\overline{R}}_{(l+1)l}(\theta_{l+1}) \cdot \overline{I}_{l+1}^{+}(\theta_{l+1}, \phi_{l+1}, z = -d_l) \tag{9}$$

$$\overline{I}_{l}^{+}(\theta_l, \phi_l, z = -d_l) = \overline{\overline{T}}_{(l+1)l}(\theta_{l+1}) \cdot \overline{I}_{l+1}^{+}(\theta_{l+1}, \phi_{l+1}, z = -d_l) + \overline{\overline{R}}_{l(l+1)}(\theta_l) \cdot \overline{I}_{l}^{-}(\pi - \theta_l, \phi_l, z = -d_l) \tag{10}$$

In the above equations (7) – (10), $0 \le \theta_l \le \pi/2$, $\overline{I}_{l}^{+}(\theta_l, \phi_l, z)$ and $\overline{I}_{l}^{-}(\pi - \theta_l, \phi_l, z)$ are used to denote the upward going intensity and downward going intensity, respectively. $\overline{\overline{T}}_{l(l+1)}(\theta_l)$ and $\overline{\overline{R}}_{l(l+1)}(\theta_l)$ are the respective transmission and reflection matrices between layers l and $l+1$ as described in Appendix. The elevation angles θ_l and θ_{l+1} in layers l and $l+1$, respectively, are related by Snell's law.

To solve radiative transfer equations using discrete-ordinate eigenanalysis method, it is required to determine a set of discrete directions appropriate to the stratified medium. The Gauss-Legendre quadrature angles are a common choice [18]. However, when we consider a layered system with a discontinuous interface of different dielectric properties, special care must be taken to connect the radiation paths across the interface between two media. To take into account the refraction across the boundary, the quadrature rule of Tanaka and Nakajima [32] is applied. Consider the interface between layer l and layer $l+1$ with $\epsilon_l < \epsilon_{l+1}$, the set of discrete angles $\mu_{(l)j}^{(I)}$, $j = 1, 2, \ldots, n$, selected in the upper layer l is connected to $\mu_{(l+1)j}^{(II)}$ in the lower layer $l+1$ by Snell's law,

$$\mu_{(l+1)j}{}^{(II)} = \sqrt{1 - (1 - \mu_{(l)j}^{(I)\,2}) \frac{\epsilon_l'}{\epsilon_{l+1}'}} \tag{11}$$

here $\mu = \cos\theta$, and ϵ_l' and ϵ_{l+1}' are the real parts of the effective permittivities of layer l and layer $l+1$, respectively. $\mu_{(l)j}^{(I)}$ are chosen to be the Gaussian quadrature angles determined from zeroes of Legendre polynomials $P_{2n}(\mu)$. A schematic diagram of the set of these discrete angles is illustrated in Figure 2. In this Snell region II, the

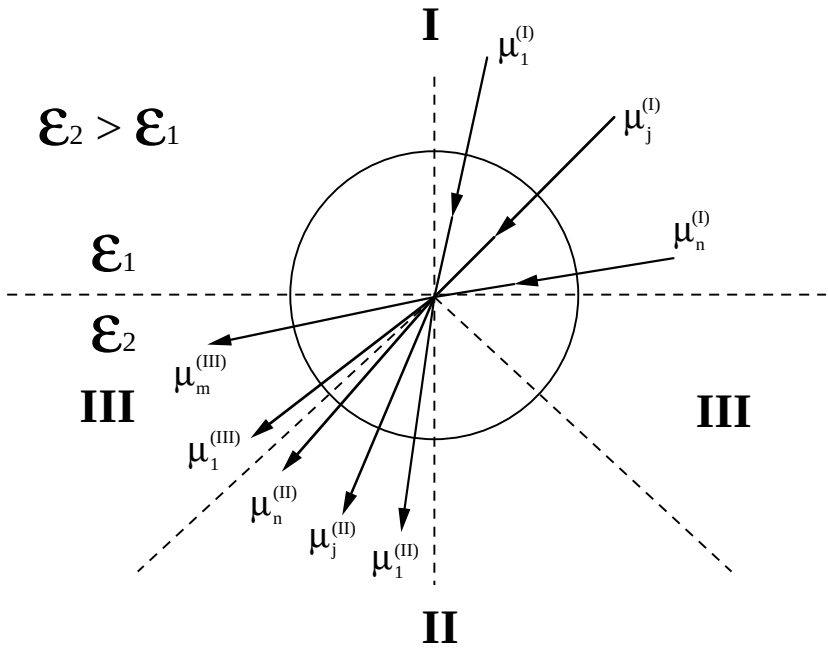

Figure 2. Schematic diagram of the set of quadrature angles. The permittivity of upper layer is smaller than lower layer ($\epsilon'_l < \epsilon'_{l+1}$). $\mu^{(I)}_{(l)j}$, $\mu^{(II)}_{(l+1)j}$, and $\mu^{(III)}_{(l+1)k}$ are the quadrature angles in layer l, Snell's region of layer $l+1$, and total reflection region of layer $l+1$, respectively.

relation between Christoffel weights $w^{(I)}_{(l)j}$ and $w^{(II)}_{(l+1)j}$ of layers l and $l+1$, respectively, can be derived as [32]

$$w^{(II)}_{(l+1)j} = \frac{\epsilon'_l \mu^{(I)}_{(l)j}}{\epsilon'_{l+1} \mu^{(II)}_{(l+1)j}} w^{(I)}_{(l)j} \tag{12}$$

To cover the total reflection region III in the lower layer ($\epsilon_{l+1} > \epsilon_l$), an additional set of m discrete angles is allocated in the region III according to

$$\mu_{(l+1)k}{}^{(III)} = \sqrt{1 - \frac{\epsilon'_l}{\epsilon'_{l+1}}}\, \mu_k \tag{13}$$

where $k = 1, \ldots, m$ and μ_k are determined as zeroes of the Legendre polynomial $P_{2m}(\mu)$. In this total reflection region, no connection be-

tween directions $\mu^{(I)}_{(l)j}$ and $\mu^{(III)}_{(l+1)k}$ need to be considered. The weights in region III are chosen as [32]

$$w^{(III)}_{(l+1)k} = \sqrt{1 - \frac{\epsilon'_l}{\epsilon'_{l+1}}}\, w_k \tag{14}$$

where w_k are the Christoffel weighting functions corresponding to μ_k. The above quadrature rule for a two-layer case can be extended to the N-layer case. Since the permittivity at each layer may not be in ascending order, an arrangement of layers is first set up such that the top layer has lowest permittivity and bottom layer has the highest permittivity. The quadrature angles and their corresponding weights in each layer is thus determined from (12)–(15) for every pair of adjacent layers. Then a re-ordering is made to restore layers to the original stratification.

3. SNTHERM MODEL SUMMARY

The ability to model the internal changes of a snowpack contributes to a better understanding of snow metamorphism. In addition, the derived snowpack structure is useful for predicting the physical properties of snow. A one-dimensional snowpack physics model known as SNTHERM [17], has been applied to a full range of winter meteorological conditions, such as snowfall, rainfall, freeze-melt cycles, and transitions between bare and snow-covered ground. This model has been used to predict changes to the optically-equivalent grain size in studies on spectral reflectance [33], summer snow melt in Arctic areas [34] and changes to snow properties under a forest canopy [35]. In this section, we describe briefly the governing equations for the energy and mass balance of snow, and the physical effects on the SNTHERM model parameters used. A detailed description of the theoretical and numerical aspects of SNTHERM is given by Jordan [17].

In SNTHERM, the snowcover is modeled as a one-dimensional (vertical coordinate z) layered system consisting of dry air, ice, liquid water and water vapor. Each layer assumes a horizontally infinite control volume which is subjected to the governing equations for energy and mass balance. The control-volume approach of Patankar [36] is adopted as a spatial discretization procedure which is similar to a finite-difference scheme. A Crank-Nicolson weighting method [17] is used for the time domain where equal weights are given to past and

current time periods. To accommodate the compaction of snowcover, the control volume thickness is allowed to change over time. The mass of ice and water is assumed to be conserved under contraction of the control volume, whereas the displaced portion of air and water vapor are expelled. Governing sets of equations are linearized with respect to the unknown variables and solved by the tridiagonal matrix algorithm [17]. At each time step, the mass balance equations are solved first and the water flux and snow density from this computation are used in the subsequent solution of the energy equation. Usually, the quarter-hourly time steps are sufficient for solution accuracy.

Boundary conditions at the air-snow interface are prescribed by meteorologicaly-determined fluxes of mass and energy:

$$F_{top} = F_s^{\downarrow}(1 - \alpha_{top}) + F_{ir}^{\downarrow} - F_{ir}^{\uparrow} + F_{sen} + F_{lat} + F_{conv} \qquad (15)$$

where the surface energy balance at the snow surface F_{top} is composed of the net solar radiation $F_s^{\downarrow}(1 - \alpha_{top})$, the net infrared radiation $F_{ir}^{\downarrow} - F_{ir}^{\uparrow}$, the turbulent fluxes of sensible F_{sen} and latent F_{lat} heat and convected heat due to snow or rain F_{conv}. The snow albedo in the solar spectral range is α_{top}, and the emitted infrared radiation $F_{ir}^{\uparrow}$ is calculated by the well-known Stefan-Boltzmann expression. The incoming solar radiation $F_s^{\downarrow}$ can be estimated as a default in the SNTHERM model, if measurements are unavailable, using Shapiro's [37, 38] method, which simplify a set of two-stream radiative transfer relations to a three-layer case. Input values rely on the solar zenith angle and cloud fraction at three heights. At each time step, SNTHERM also provides a default estimate of the incoming infrared radiation $F_{ir}^{\downarrow}$ [17, 39], which is driven by measurements of air temperature and humidity at a reference height, in the case where measurements are unavailable.

SNTHERM requires initial vertical profiles of temperature, water content, grain size, and density for the snowpack. These physical characteristics for the selected strata are usually supplied from real measurements. With the subsequent meteorological conditions (air temperature and humidity, wind speed, precipitation, solar and infrared radiation), SNTHERM provides various outputs including depth profiles of snow properties, surface energy flux, and water infiltration. Among them, the stratified structure of snow layers, grain size, bulk snow density and liquid density are the required parameters for DMRT scattering model.

Densification of a snow layer is represented in SNTHERM by the combination of the compaction rate and the mass balance of the layer. If the snow is dry, the mass balance incorporates grain growth, and if the snow is wet, liquid water movement is taken into account as well [17]. Therefore, the time rate of change of the density of snow depends on compaction, which is a function of the overburden, grain growth and liquid water content. The grain growth algorithm for dry snow is an adaptation of a function used to predict growth by sintering in metals and ceramics.

$$4\frac{\partial a_l}{\partial t} = \frac{g1|U_v|}{a_l} = \frac{g1}{a_l} D_s \left(\frac{1000}{P_a}\right) \left(\frac{T}{273.16}\right)^6 C_{kT} \left|\frac{\partial T}{\partial z}\right| \qquad (16)$$

where t is time, $g1$ is a fitting parameter based on grain growth experiments [17], and U_v is the mass vapor flux in the snow, taken as a purely diffusive process, parallel to sensible heat conduction, and calculated with Fick's Law. The effective diffusion for water vapor in snow is D_s, P_a is atmospheric pressure, T is the snow temperature and C_{kT} is the variation of saturation vapor pressure with temperature relative to phase. Grain growth thus increases with increasing temperature gradient, but slows as the grains become larger.

If the snow is wet, grain growth depends on the liquid water saturation regime, which in turn depends on the liquid water content, pendular or funicular [30]. The saturation regimes also controls the shape of the liquid water inclusions in the snow grain matrix, which in turn controls the depolarization factor [30]. The two grain-growth functions are similar to those used for dry snow:

$$4\frac{\partial a_l}{\partial t} = \frac{g2}{a_l} (f_{vl} + 0.05) \qquad (17)$$

when $0.00 < f_{vl} < 0.09$ and

$$4\frac{\partial a_l}{\partial t} = \frac{g2}{a_l} (0.14) \qquad (18)$$

when $f_{vl} \geq 0.09$. The adjustable parameter $g2$, based on laboratory data [17], was set at $4.0 \times 10^{-12} m^2/s$. The liquid water content obtains from the combination of an infiltration-exfiltration term for each layer, and the sink-source term due to phase change between ice and liquid water. We assume gravity dominates the movement of liquid water

and retention by a layer is inversely proportional to grain size a_l and directly proportional to porosity [17].

Table 1 presents a partial listing of a SNTHERM output file for a wet snow case. It shows that the temperature, density, size, and wetness varies with the snow depth, and the snowpack does contain snow at various states of metamorphosis.

layer thickness (cm)	snow density (kg/m^3)	liquid density (kg/m^3)	grain diameter (m)	temperature ($^\circ K$)
2	296.7377	39.93511	0.001018	273.1245
2	280.1065	41.71200	0.001020	273.1264
2	233.8583	43.63070	0.001021	273.1290
2	260.1276	39.73432	0.001696	273.1263
2	255.1933	33.53677	0.002010	273.1234
2	184.2652	15.35970	0.002010	273.1170
2	210.5205	3.896910	0.002009	272.2266
2	222.6257	0.012070	0.002008	271.6794
2	231.6061	0.005000	0.002004	270.9930

Table 1. Sample SNTHERM output file.

4. COMPARISON OF MODEL AND MEASUREMENTS

A series of millimeter wave backscatter experiments on snowcover were conducted by the University of Massachusetts at Amherst, details of experimental procedures and observations are given in [15, 16]. Three radar systems operating at 35, 95, and 225 GHz were used in the experiment, where the 95 and 225 GHz radars are fully polarimetric, while the 35 GHz one was only capable of vv polarization observations. Besides the radar signatures, meteorological data and snow ground truth were also recorded. The meteorological measurements included air temperature, wind speed and relative humidity. Supplemental data on cloud cover, to estimate the solar radiation, was acquired from a nearby airport. Ground truth measurements of snow included snow depth, liquid water content, temperature, snow density, grain size, and snow layer thickness. Samples of snow were also collected for plane section analysis [6, 7] to estimate the volume-weighted scatterer size a_l. Measurements reported in earlier experiments [15, 16] measured

the maximum dimension of particles as the grain size. Measurements with the 35 and 95 GHz radars showed strong diurnal variations during the period of 1 March (Day 60) 1993 to 8 March (Day 67) 1993. The model simulations presented in the following will focus on these two sets of radar data and the concurrently measured meteorological conditions and snow ground truth.

4.1 SNTHERM Simulations

We carried out the SNTHERM simulation for the whole eight-day period with meteorological data (air temperature, relative humidity, wind speed, cloud cover, and precipitation) at hourly intervals measured from a close by weather station. The measurement period began with 20 cm of metamorphosized snow that had undergone several freeze-thaw cycles. Three freeze-melt cycles were experienced from Day 60 to Day 62 under mostly clear skies. There was also a slight freeze-melt event on Day 63 under cloudy sky. The snowpack compacted to depths of 17.5 cm and 15 cm during Day 61 and Day 62, respectively. A light snowfall began at the end of Day 63, 2 cm of fresh snow was gained by the morning of Day 64. Additional snowfall during Day 64 provided 15 cm of dry snowcover. A cumulated snow height of 30 cm was on the ground of Day 65. Freeze-melt cycles then reduced the snow depths to 25 cm and 20 cm during Day 65 and Day 66, respectively.

Table 2 presents the snow property profile used to initiate the model run in this study. Field measurements provided the snow density and grain size, while a stratigraphic description guided selection of the layer intervals. We estimated the temperatures to mimic a night time profile. Precipitation and compaction modulated the total depth during the simulation. The input precipitation files derived from measurements of snowfall on the test field. We used no updates; the model ran forward through the time period Day 60 to 67.

Figure 3 shows predicted and measured snow depths, plotted as a time series. In almost every case, the SNTHERM predicted about 10 percent less depth than the measurements taken over the test field. We believe that both a low estimate of the initial snow depth and an over-predicted compaction rate explain the discrepancies. Nonetheless, the overall time trend of the snow depth appears well predicted. Figure 4 plots predicted snow densities and measured snow densities for the test period. Agreement appears good at low to moderate densities. Greater scatter occurs at higher densities, where SNTHERM tends to

over-predict densification rates. This is consistent with the snow depth comparison in Figure 3.

layer thickness (cm)	snow density (kg/m^3)	liquid density (kg/m^3)	grain diameter (m)	temperature ($^\circ K$)
1	328	0.00	0.0010	271.15
2	271	0.00	0.0010	271.15
2	246	0.00	0.0010	271.65
3	189	0.00	0.0010	271.65
3	233	0.00	0.0020	272.15
3	162	0.00	0.0020	272.15
3	217	0.00	0.0020	271.15
3	230	0.00	0.0020	271.15

Table 2. Initial parameters for SNTHERM simulation.

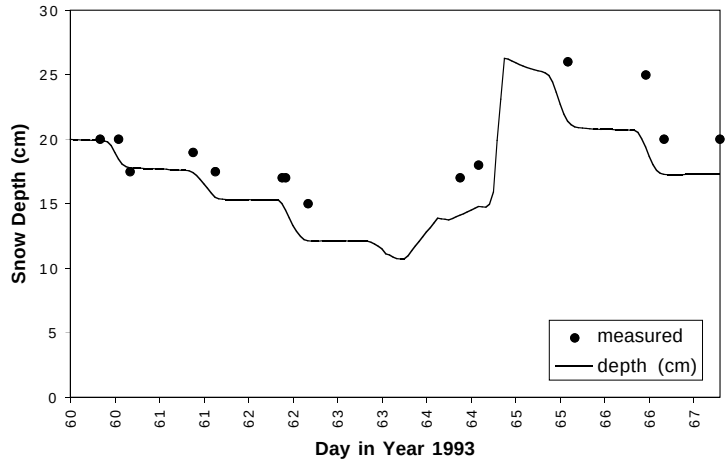

Figure 3. Time series of snow depth simulated with SNTHERM and measurements. SNTHERM predictions incorporate settlement, compaction and melting of the snow, as well as accumulation during stormy period.

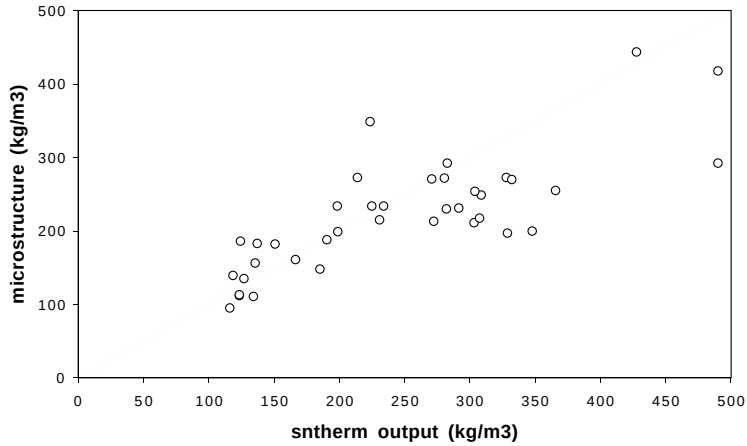

Figure 4. Comparison of predicted snow densities and measured snow densities for all ground truth measurements. Good agreement can be seen for the density range most representative of the conditions during the experiment.

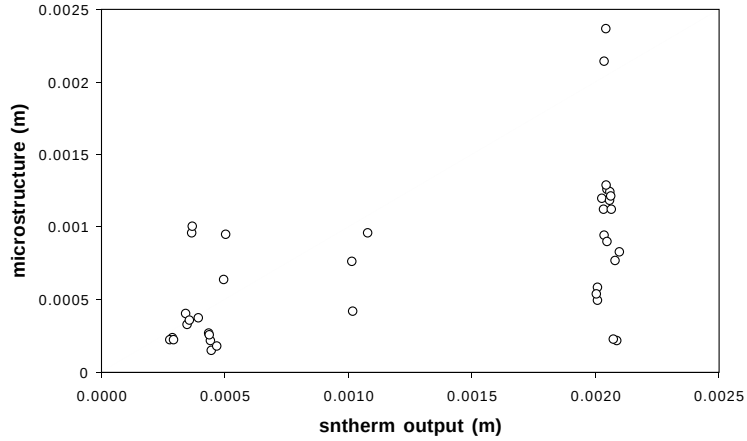

Figure 5. Comparison of predicted grain sizes with those measured from section analysis of preserved snow specimens.

Figure 5 shows comparison of grain sizes predicted by SNTHERM and grain sizes obtained from section analysis [6, 7]. SNTHERM was initialized (Table 2) with grain sizes equivalent to the volume-weighted sphere, determined from the mean ice intercepts [7]. This grain size, while appropriate for microwave and millimeter-wave modeling [7], causes an under-prediction of the snow albedo α_{top} [33]. This effect, in turn, causes a higher net energy input to the snow cover (Eq. 15) and a slightly higher compaction rate. The volume-weighted grain size [7] assumes a log-normal distribution of particle sizes in the snow cover. SNTHERM predicts the growth of a single grain size (Eqs. 16-18) and therefore cannot account for changes to the size distribution of grains in the snow cover. The agreement between prediction and measurement seems fair at the smaller grain sizes, but SNTHERM over predicted grain size in the larger size classes. These grains were generally found near the base of the snow cover, and hence do not have a strong effect on high-angle millimeter-wave backscatter.

4.2 DMRT Simulations

We perform the backscatter simulations of snowcover with the snow parameters, density, grain size, wetness, and layer thickness, as provided by SNTHERM or ground truth measurements. Typical values of ice permittivity $\epsilon_s = (3.2 + i0.002)\epsilon_0$ and soil permittivity $\epsilon_g = (6.0 + i0.6)\epsilon_0$ are assumed; however, the stickiness parameter is chosen to be $\tau = 0.2$, throughout the whole simulation.

Figure 6 shows the 35 GHz backscattering coefficients σ_{vv} as a function of incident angle. The symbols represent the data measured at the early morning of Day 63 from a layer of dry snow. The *in situ* measured snow parameters are $d_1 = 6cm$, $d_2 = 9cm$, $a_1 = 0.49mm$, $a_2 = 0.53mm$, $f_{v1} = 0.37$, $f_{v2} = 0.22$, and without sensible wetness [16]. It is noted that, with these snow parameters, real parts of the effective permittivities calculated from (3) are $\epsilon_1' = 1.64\epsilon_0$ and $\epsilon_2' = 1.34\epsilon_0$ which are quite different from each other. A two-layer DMRT model of snow is first used, and the solid curve in Figure 6 shows the model result which agrees quite well with the radar data. However, if we artificially ignore the discontinuity of effective dielectric constants between the two layers, *i.e.*, with full transmission and null reflection in (9) and (10), the simulated backscatter are represented by the dashed curve in Figure 6. A lower σ_{vv}, without the inclusion of reflection and refraction between the snow-snow interface, is observed. If we further

use a hard sphere model (without surface bonding), the simulation results, shown as the dotted curve in Figure 6, are noticed with a large deviation from measured backscattering coefficients. It indicates the importance of considering the collective scattering effects due to particles in proximity within a cluster. Using the snow parameters (Table 3) provided by the SNTHERM model, the simulation results with a 6-layer snow model are shown in Figure 6 by a dash-dotted curve. It shows a better agreement with measured data using the coupled DMRT and SNTHERM model.

Figure 7 presents the model and the measured backscatter of σ_{vv} at 35 GHz and 60° incident angle for the whole period of data collection. The comparisons of measured and simulated backscattering coefficients of σ_{vv}, σ_{hh}, and σ_{hv} for 95 GHz and 60° incident angle are illustrated in Figures 8, 9, and 10, respectively. The snow parameters are all supplied by the SNTHERM simulations. The temporal responses of DMRT are at hourly intervals. The observed strong diurnal variation of radar response is correlated with the liquid water content within the snowpack. The backscatter drops during daytime periods when liquid water content increases, while in cold nights, the backscatter rises back again because of the refreezing of the snow. The drop of backscatter at 35 GHz is larger than that at 95 GHz during freeze-thaw cycles. It can be seen that the model predictions are, in general, consistent with the measured data in both timing and magnitude. Both measured and model radar responses at 35 and 95 GHz show a quick drop at the onset of melting as a result of the presence of liquid water during the warm daytime. Due to water infiltration, the liquid water has a nonuniform distribution in the snowpack. As refreezing occurs in the cold night, the good insulation property of snow slows down the refreezing process in deeper layers, thus causing a slow recovery of the backscatter. For 95 GHz, due to the small penetration depth and large scattering effect, the diurnal variations are not as significant as 35 GHz response. However, the model simulation predicts a slower rise than measurements in backscatter as refreezing occurs, which may due regard to overestimated liquid water content or slower refreezing prediction in the SNTHERM model.

layer thickness (cm)	snow density (kg/m^3)	liquid density (kg/m^3)	grain diameter (m)
2	285.6801	0.028502	0.001566
2	280.1921	0.451180	0.002044
2	279.9320	3.823100	0.002041
2	322.0839	0.527608	0.003043
2	368.7351	0.024953	0.002039
2	427.1245	0.013300	0.002032

Table 3. SNTHERM simulated snow parameters at Hour 01, Day 63.

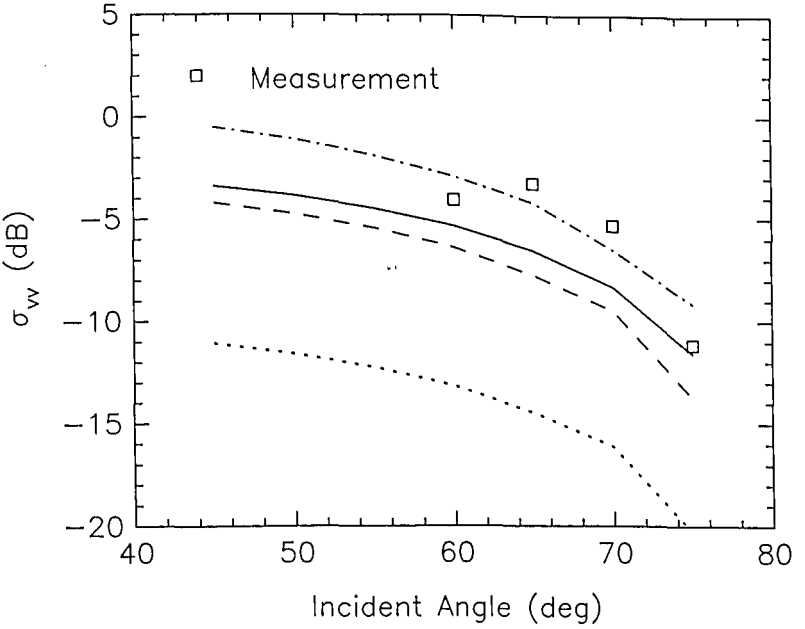

Figure 6. Comparison of theoretical simulations with snow measured data in vv polarization at 35 GHz. □ represents measured data [15]. $\cdots$ is the 2-layer DMRT model result with hard sphere model and without considering reflection and refraction at snow-snow interface. $- - -$ is the DMRT simulation result using sticky hard sphere model with stickiness $\tau = 0.2$ but without considering reflection and refraction at snow-snow interface. —— is the simulation with stickiness $\tau = 0.2$ and considering snow-snow interface effect. $-\cdot-\cdot-$ represents 6-layer DMRT model result using snow parameters from SNTHERM simulation.

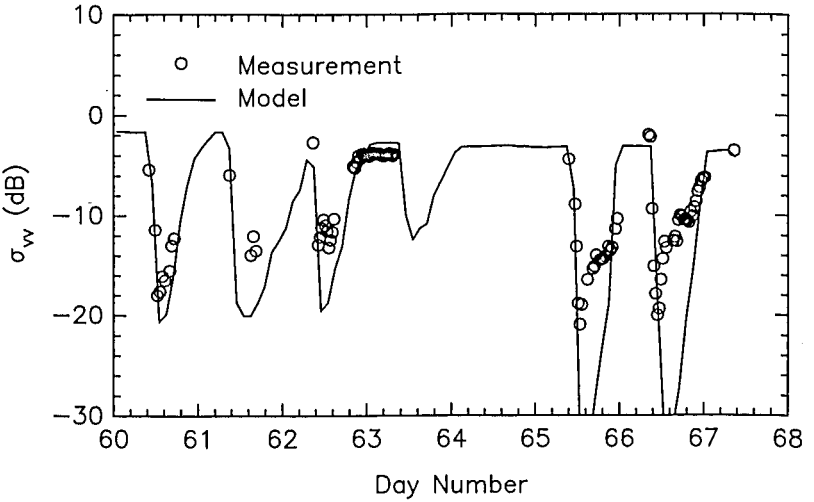

Figure 7. Temporal variations of backscatter in *vv* polarization at 35 GHz and 60° incident angle. Circles are measured data from Reference [16] and solid curve is DMRT simulation with snow parameters provided by SNTHERM model.

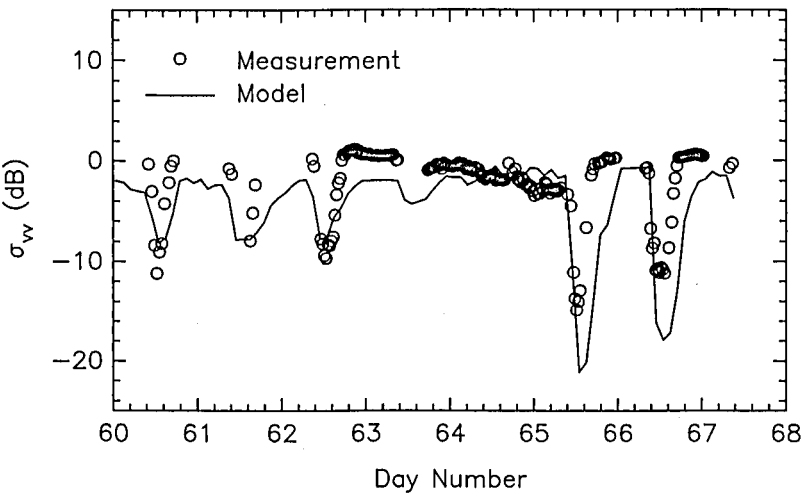

Figure 8. Temporal variations of backscatter in *vv* polarization at 95 GHz and 60° incident angle. Circles are measured data from Reference [16] and solid curve is DMRT simulation with snow parameters provided by SNTHERM model.

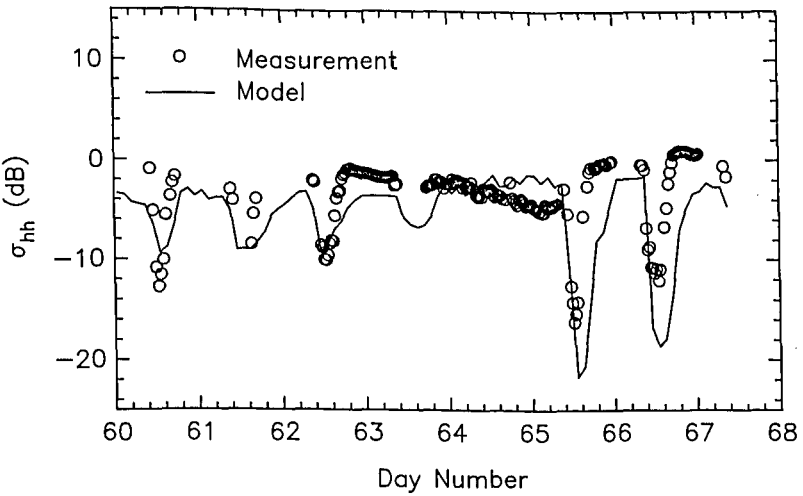

Figure 9. Temporal variations of backscatter in *hh* polarization at 95 GHz and 60° incident angle. Circles are measured data from Reference [16] and solid curve is DMRT simulation with snow parameters provided by SNTHERM model.

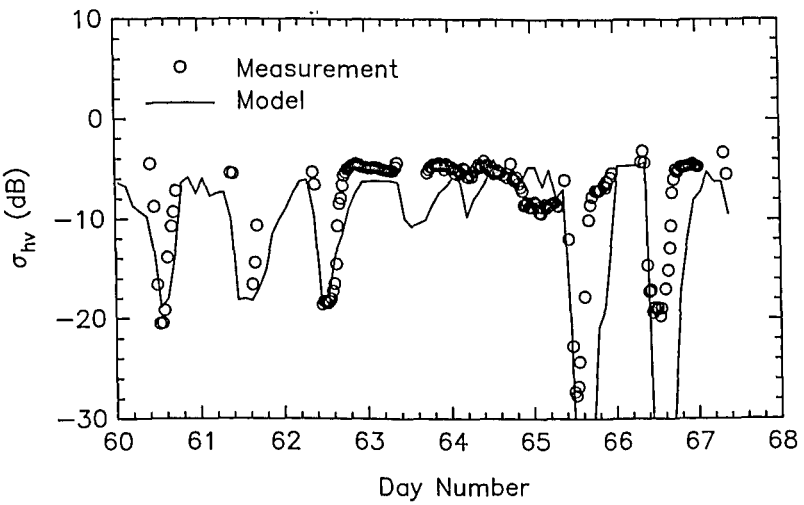

Figure 10. Temporal variations of backscatter in *hv* polarization at 95 GHz and 60° incident angle. Circles are measured data from Reference [16] and solid curve is DMRT simulation with snow parameters provided by SNTHERM model.

5. SUMMARY

In this work we present a millimeter wave backscatter model of time-varying snowcover. This model is developed based on the multilayer DMRT theory with an one-dimensional snowpack physics model named SNTHERM. The electromagnetic sensor response of snowcover is calculated by solving the multilayer DMRT equations, where the cohesive spherical particles are used to model the metamorphosed snow grains, and the effects of reflection and refraction at the snow-snow interface are taken into account. The SNTHERM model is applied to study the influence of surface energy exchange under varying meteorological conditions on the snow metamorphosis process. It supplies important snow model parameters, and in this case was used to interpolate in time the snow property measurements made in the field and laboratory. We demonstrated that SNTHERM can provide the linkage between the snow metamorphosis and the electromagnetic properties of snowcovers. The resulting backscatter from coupled multilayer DMRT and SNTHERM model is compared with experimental data and good agreements are obtained. It indicates this coupled multilayer DMRT and SNTHERM model can be useful in predicting the multi-temporal radar response of snowcovers and in retrieving snow parameters for remote sensing applications.

ACKNOWLEDGMENT

The research in this paper was supported by the U.S. Army Cold Regions Research and Engineering Laboratory Contract No. DACA89-95-K-0014, the Office of Naval Research Contract No. N00014-92-J-4098, and US Army Project 4A762784AT42.

APPENDIX

In this appendix we give the reflection matrix $\overline{\overline{R}}_{l(l+1)}(\theta_l)$ and transmission matrix $\overline{\overline{T}}_{l(l+1)}(\theta_l)$ between layers l and $l+1$ described in Section 2.2.

$$\overline{\overline{R}}_{l(l+1)}(\theta_l) = \begin{bmatrix} r_{v_{l(l+1)}} & 0 & 0 & 0 \\ 0 & r_{h_{l(l+1)}} & 0 & 0 \\ 0 & 0 & W_{l(l+1)} & -Z_{l(l+1)} \\ 0 & 0 & Z_{l(l+1)} & W_{l(l+1)} \end{bmatrix} \tag{A.1}$$

$$\overline{\overline{T}}_{l(l+1)}(\theta_l) = \frac{\epsilon'_{l+1}}{\epsilon'_l} \begin{bmatrix} t_{v_{l(l+1)}} & 0 & 0 & 0 \\ 0 & t_{h_{l(l+1)}} & 0 & 0 \\ 0 & 0 & g_{l(l+1)} & -h_{l(l+1)} \\ 0 & 0 & h_{l(l+1)} & g_{l(l+1)} \end{bmatrix} \tag{A.2}$$

where

$$r_{v_{l(l+1)}} = |S_{l(l+1)}|^2 \tag{A.3}$$

$$r_{h_{l(l+1)}} = |R_{l(l+1)}|^2 \tag{A.4}$$

$$W_{l(l+1)} = Re(S_{l(l+1)} R^*_{l(l+1)}) \tag{A.5}$$

$$Z_{l(l+1)} = Im(S_{l(l+1)} R^*_{l(l+1)}) \tag{A.6}$$

and

$$t_{v_{l(l+1)}} = 1 - r_{v_{l(l+1)}} \tag{A.7}$$

$$t_{h_{l(l+1)}} = 1 - r_{h_{l(l+1)}} \tag{A.8}$$

$$g_{l(l+1)} = \frac{\cos\theta_{l+1}}{\cos\theta_l} Re(Y_{l(l+1)} X^*_{l(l+1)}) \tag{A.9}$$

$$h_{l(l+1)} = \frac{\cos\theta_{l+1}}{\cos\theta_l} Im(Y_{l(l+1)} X^*_{l(l+1)}) \tag{A.10}$$

for θ_l less than the critical angle, otherwise

$$g_{l(l+1)} = h_{l(l+1)} = 0 \tag{A.11}$$

and

$$X_{l(l+1)} = 1 + R_{l(l+1)} \tag{A.12}$$

$$Y_{l(l+1)} = 1 + S_{l(l+1)} \tag{A.13}$$

where $R_{l(l+1)}$ and $S_{l(l+1)}$ are the respective TE and TM Fresnel reflection coefficients, and ϵ'_l and ϵ'_{l+1} are the real parts of permittivities at layers l and $l+1$, respectively [18].

REFERENCES

1. Cohen, J., and D. Rind, "The effect of snow cover on the climate," *J. Climate,* Vol. 4, No. 7, 689–706, 1991.
2. Rango, A., "Progress in snow hydrology remote-sensing research," *IEEE Trans. Geosci. Remote Sensing,* Vol. GE-24, No. 1, 47–53, 1986.

3. Dozier, J., "Recent research in snow hydrology," *Rev. Geophys.*, Vol. 25, No. 2, 153–161, 1987.
4. Colbeck, S. C., "The layered character of snow covers," *Rev. Geophys.*, Vol. 29, No. 1, 81–96, 1991.
5. Arons, E. M., and S. C. Colbeck, "Geometry of heat and mass transfer in dry snow: a review of theory and experiment," *Rev. Geophys.*, Vol. 33, No. 4, 463–493, 1995.
6. Davis, R. E., and J. Dozier, "Stereological characterization of dry Alpine snow for microwave remote sensing," *Adv. Space Res.*, Vol. 9, No. 1, 245–251, 1989.
7. Shi, J., R. E. Davis, and J. Dozier, "Stereological determination of dry-snow parameters for discrete-scatterer microwave modeling," *Ann. Glaciol.*, Vol. 17, 295–299, 1993.
8. Stiles, W. H., and F. T. Ulaby, "The active and passive microwave response to snow parameters 1. wetness," *J. Geophys. Res.*, Vol. 85, No. C2, 1037–1044, 1980.
9. Baars, E. P., and H. Essen, "Millimeter-wave backscatter measurements on snow-covered terrain," *IEEE Trans. Geosci. Remote Sensing,* Vol. 26, No. 3, 282–299, 1988.
10. Williams, L. D., J. G. Gallagher, D. E. Sugden, and R. V. Birnie, "Surface snow properties effects on millimeter-wave backscatter," *IEEE Trans. Geosci. Remote Sensing,* Vol. 26, No. 3, 300–306, 1988.
11. Currie, N. C., J. D. Echard, M. J. Gary, A. H. Green, T. L. Lane, and J. M. Trostel, "Millimeter-wave measurements and analysis of snow-covered ground," *IEEE Trans. Geosci. Remote Sensing,* Vol. 26, No. 3, 307–318, 1988.
12. Narayanan, R. M., and R. E. McIntosh, "Millimeter-wave backscatter characteristics of multilayered snow surfaces," *IEEE Trans. Antennas Propagat.*, Vol. 38, No. 5, 693–703, 1990.
13. Mead, J. B., P. S. Chang, S. P. Lohmeier, P. M. Langlois, and R. McIntosh, "Polarimetric observations and theory of millimeter-wave backscatter from snow cover," *IEEE Trans. Antennas Propagat.*, Vol. 41, No. 1, 38–46, 1993.
14. Ulaby, F. T., T. F. Haddock, R. T. Austin, and Y. Kuga "Millimeter-wave radar scattering from snow: 2. comparison of theory with experimental observations," *Radio Sci.*, Vol. 26, No. 2, 343–351, 1991.
15. Chang, P. S., "Observation and theory of polarimetric backscatter from snowcover at 35, 95 and 225 GHz," Ph.D. dissertation, University of Massachusetts, 1994.
16. Chang, P. S., J. B. Mead, E. J. Knapp, G. A. Sadowy, R. E. Davis, and R. E. McIntosh, "Polarimetric backscatter from fresh

and metamorphic snowcover at millimeter wavelengths," *IEEE Trans. Antennas Propagat.*, Vol. 44, No. 1, 58–73, 1996.
17. Jordan, R., "A one-dimensional temperature model for a snow cover: Technical documentation for SNTHERM.89," *Spec. Rep. 91-16,* U.S. Army Corps of Eng., Cold Reg. Res. and Eng. Lab., Hanover, N.H., 1991.
18. Tsang, L., J. A. Kong, and R. T. Shin, *Theory of Microwave Remote Sensing.* Wiley-Interscience, New York, 1985.
19. Twersky, V., "Coherent electromagnetic waves in pair-correlated random distributions of aligned scatterers," *J. Math. Phys.*, Vol. 19, No. 1, 215–230, 1978.
20. Ishimaru, A., and Y. Kuga, "Attenuation constant of a coherent field in a dense distribution of particles," *J. Opt. Soc. Am.*, Vol. 72, No. 10, 1317–1320, 1982.
21. Koh, G., "Experimental study of electromagnetic wave propagation in dense random media," *Waves Random Media,* Vol. 2, No. 1, 39–48, 1992.
22. Tsang, L., C. E. Mandt, and K. H. Ding, "Monte Carlo simulations of the extinction rate of dense media with randomly distributed dielectric spheres based on solution of Maxwell's equations," *Opt. Lett.*, Vol. 17, No. 5, 314–316, 1992.
23. Tsang, L., and A. Ishimaru, "Radiative wave equations for vector electromagnetic propagation in dense nontenuous media," *J. Electro. Waves Applic.*, Vol. 1, No. 1, 59–72, 1987.
24. Tsang, L., "Dense media radiative transfer theory for dense discrete random media with particles of multiple sizes and permittivities," *Progress in Electromagnetics Research, Volume 6.* New York: Elsevier, Ch. 5, 181–230, 1992.
25. Wen, B., L. Tsang, D. P. Winebrenner, and A. Ishimaru, "Dense medium radiative transfer theory: comparison with experiment and application to microwave remote sensing and polarimetry," *IEEE Trans. Geosci. Remote Sensing,* Vol. 28, No. 1, 46–59, 1990.
26. West, R., L. Tsang, and D. P. Winebrenner, "Dense medium radiative transfer theory for two scattering layers with a Rayleigh distribution of particle sizes," *IEEE Trans. Geosci. Remote Sensing,* Vol. 31, No. 2, 426–437, 1993.
27. Ding, K. H., L. M. Zurk, and L. Tsang, "Pair distribution functions and attenuation rates for sticky particles in dense media," *J. Electro. Waves and Applic.*, Vol. 8, No. 12, 1585–1604, 1994.
28. Zurk, L. M., L. Tsang, K. H. Ding, and D. P. Winebrenner, "Monte Carlo simulations of the extinction rate of densely packed spheres with clustered and nonclustered geometries," *J. Opt. Soc. Am. A.*, Vol. 12, No. 8, 1772–1781, 1995.

29. Zurk, L. M., L. Tsang, and D. P. Winebrenner, "Scattering properties of dense media from Monte Carlo simulations with applications to active remote sensing of snow," *Radio Sci.,* Vol. 31, No. 4, 803–819, 1996.
30. Hallikainen, M., F. T. Ulaby, and M. Abdelrazik, "Dielectric properties of snow in the 3 to 37 GHz range," *IEEE Trans. Antennas Propagat.,* Vol. AP-34, No. 11, 1329–1340, 1986.
31. Sihvola, A. H., and J. A. Kong, "Effective permittivity of dielectric mixtures," *IEEE Trans. Geosci. Remote Sensing,* Vol. 26, No. 4, 420–429, 1988.
32. Tanaka, M., and T. Nakajima, "Effects of oceanic turbidity and index of refraction of hydrosols on the flux of solar radiation in the atmosphere-ocean system," *J. Quant. Spectrosc. Radiat. Transfer,* Vol. 18, No. 1, 93–111, 1977.
33. Davis, R. E., A. W. Nolin, R. Jordan, and J. Dozier, "Towards predicting temporal changes of the spectral signature of snow in visible and near infrared wavelengths," *Annals of Glaciol.,* Vol. 17, 143–148, 1993.
34. Rowe, C. M., K. C. Kuiven, and R. Jordan, "Simulation of summer snowmelt on the Greenland ice sheet using a one-dimensional model," *J. Geophys. Res.,* Vol. 100, No. D8, 16265–16273, 1995.
35. Hardy, J. P., R. E. Davis, R. Jordan, X. Li, C. Woodcock, W. Ni, and J. C. McKenzie, "Snow ablation modeling at the stand scale in a boreal jack pine forest," *J. Geophys. Res.* in press.
36. Patankar, S. V., *Numerical Heat Transfer and Fluid Flow,* New York: Hemisphere Publishing, 1980.
37. Shapiro, R., "Solar radiative flux calculations from standard surface meteorological observations," *Report AFGL-TR-83-0039,* Systems and Applied Sciences Corporation, Riverdale MD, AF Geophysics Laboratory, 1982.
38. Shapiro, R., "A simple model for the calculation of the flux of direct and diffuse solar radiation through the atmosphere," *Report AFGL-TR-87-0200,* ST Systems Corporation, Lexington MA, AF Geophysics Laboratory, 1987.
39. Idso, S. B., "A set of equations for full spectrum and 8–14 μm and 10.5–12.5 μm thermal radiation from cloudless skies," *Water Resources Res.,* Vol. 17, No. 2, 295–304, 1981.